
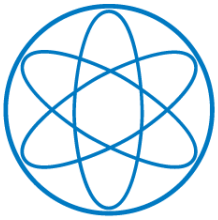
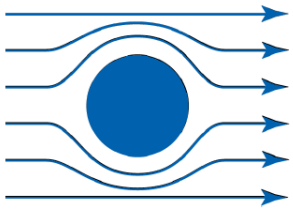

Technische Universität München

Fakultät für Physik

Walther-Meißner-Institut für Tieftemperaturforschung

Abschlussarbeit im Bachelorstudiengang Physik

Broadband Ferromagnetic Resonance Setup

Aufbau für Breitbandige Ferromagnetische Resonanz

Johannes Küchle

20. Juli 2015

Themensteller: PD Dr. Sebastian T. B. Gönnenwein

Zweitgutachter: Prof. Dr. Peter Böni

Contents

1 Introduction

Ferromagnetic resonance (FMR) is the resonant absorption of electromagnetic waves in a system of coupled magnetic moments. It appears if a ferromagnet is placed in a static magnetic field and a to the sample perpendicular microwave field is applied.

For each microwave frequency there is a correlated static magnetic field where the FMR occurs. Determining this static field for several microwave frequencies is referred to as broadband ferromagnetic resonance. The most important parameters for ferromagnets, such as the magnetic anisotropies, the Lande g-factor or the Gilbert-damping, can be deduced by broadband FMR. These values are of huge importance for technical advance, e.g. in the information technology, where the requested velocity and the miniaturization overburden the conventional electronic. Therefore, FMR studies have been increasing since the discovery of electron paramagnetic resonance in 1945 [1].

In this thesis, I focused on the implementation of a setup for broadband FMR measurements and its applications. Two measurement setups are used: on the one hand, a vector network analyzer and on the other hand, a lock-in amplifier. We start with the investigation of several waveguides. These deliver the microwave field to the sample. For an Yttrium Iron Garnet (YIG, $Y_3Fe_5O_{12}$) sample, the effective magnetization M_{eff}, the gyromagnetic ratio γ, the Lande g-factor g as well as the damping parameter α and the inhomogeneous broadening ΔH_0 are evaluated using the vector network analyzer setup. Subsequently, two important measurement parameters for the setup based on lock-in detection, the microwave power and the frequency modulation depth of the microwave source, are discussed and determined for a YIG sample. An appropriate choice of these parameters is a "tightrope walk" between clear signals and distorted results. Finally, the distance between the sample and the waveguide has been varied and its influence on the line width determined.

2 Fundamentals

2.1 Theoretical Basics

In this chapter, we introduce the theoretical aspects for the experiments and the results.

The Hamiltonian of a spin in an external magnetic flux density B_0, oriented along the z-axis, is given by:

$$\hat{\mathcal{H}} = g\mu_B B_0 \hat{S}_z \tag{1}$$

in which g is the Lande g-factor ($g \approx 2$), $\mu_B = \frac{e\hbar}{2m_e} = 9.274 \cdot 10^{-24}\text{J/T}$ is the Bohr magneton and $\hat{S}_z$ is the z-component of the electron spin vector operator. The spin can absorb microwaves if the energy of the microwaves fulfills the resonance condition [2]:

$$\hbar\omega_{\text{MW}} = g\mu_B B_0 \tag{2}$$

in which $\hbar = \frac{h}{2\pi} = 1.05457 \cdot 10^{-34}\text{Js}$ is the reduced Planck constant. However, the spins are not isolated in ferromagnetic or ferrimagnetic materials. The individual spins are coupled by the exchange interaction [3]. Therefore, S_z can be replaced by the macroscopic magnetization $\mathbf{M}$. Furthermore, the external flux density B_0 is to be replaced by the sum of all internal and external fields, which is referred to as effective field $\mu_0\mathbf{H}_{\text{eff}}$.

In this case, the equation of motion of the magnetization of a spin can be described by the Landau–Lifshitz–Gilbert (LLG) equation [4]:

$$\frac{\partial \mathbf{m}}{\partial t} = -\gamma \mathbf{m} \times \mu_0 \mathbf{H}_{\text{eff}} + \alpha\ \mathbf{m} \times \frac{\partial \mathbf{m}}{\partial t} \tag{3}$$

with the unit vector of magnetization direction $\mathbf{m} = \frac{\mathbf{M}}{M_s}$, the gyromagnetic ratio $\gamma = g\frac{\mu_B}{\hbar}$ and a phenomenological damping parameter α (Gilbert parameter). $\mathbf{H}_{\text{eff}}$ consists of the external field $\mathbf{H}$, the demagnetization field $\mathbf{H}_{\text{demag}}$ and the anisotropy $\mathbf{H}_{\text{k}}$: $\mathbf{H}_{\text{eff}} = \mathbf{H}+\mathbf{H}_{\text{demag}}+\mathbf{H}_{\text{k}}$. Two forces act on the magnetic moment: the precession force $\mathbf{F}_1 \propto \mathbf{m} \times \mathbf{H}_{\text{eff}}$ and the damping force $\mathbf{F}_2 \propto \mathbf{m} \times \frac{\partial \mathbf{m}}{\partial t}$. $\mathbf{F}_1$ causes the spin to precess around is equilibrium position and $\mathbf{F}_2$ moves the spin back to the equilibrium position, as shown in Fig. 1. Normally, $\mathbf{F}_2$ is much smaller than $\mathbf{F}_1$ (e.g. $\alpha_{Iron} \approx 0.0019$), so that $\frac{\partial \mathbf{m}}{\partial t} \approx \mathbf{F}_1$ and $\mathbf{M}$ precesses about $\mathbf{H}_{\text{eff}}$.

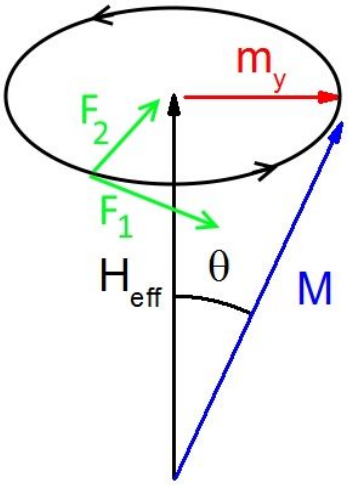

Figure 1: Schematic depiction of $\mathbf{M}$ precession around the effective field $\mathbf{H}_{\text{eff}}$. θ is the precession cone angle and $\mathbf{m}_y$ is the dynamic component of m along the y axis. The forces $\mathbf{F}_1$ (precession) and $\mathbf{F}_2$ (damping) are derived from the LLG (3).

The magnetic response of a ferromagnet to small time-varying magnetic fields, perpendicular to m, is described by the susceptibility χ. For the out-of-plane (oop) configuration, in which the static magnetic field is perpendicular to the sample plane, the susceptibility can be derived following the LLG (3) [5]:

$$\chi_{\text{oop, }yy} = \frac{M_s(\mathbf{H} - \mathbf{M}_{\text{eff}})}{(\mathbf{H} - \mathbf{M}_{\text{eff}})^2 - \mathbf{H}_{\text{eff}}^2 - i\Delta H(\mathbf{H} - \mathbf{M}_{\text{eff}})} \tag{4}$$

with $\mathbf{H}_{\text{eff}} \doteq \frac{2\pi f}{\gamma \mu_0}$ and $\mathbf{M}_{\text{eff}} = M_{\text{s}} - H_{\text{k}}$, with the saturation magnetization M_{s} and the out-of-plane anisotropy field H_{k}.

Based on Fig. 1, we define the precession cone angle θ between $\mathbf{M}$ and $\mathbf{H}_{\text{eff}}$, which describes the deflection of the spin. The deflection is given by the angle between the equilibrium position and the deflected position

$$\theta = \sin\left(\frac{\mathbf{m}_y}{\mathbf{M}}\right) \tag{5}$$

Its magnitude is defined by the power of the microwave field, which is set by the microwave source, and drives the magnetic moment out of its equilibrium position.

Measuring the microwave transmission as a function of the applied external field for a fixed microwave frequency, a resonant absorption for a specific external field can be seen when the field fulfills the resonance condition of Eq. (2).

For the fundamental mode, also referred to as ferromagnetic resonance (FMR), the Kittel

equation [6] defines the resonance microwave frequency for a given static magnetic field:

$$\omega_0^2 = \gamma^2[B_0 + (N_y - N_z)\mu_0 M_{\text{eff}}][B_0 + (N_x - N_z)\mu_0 M_{\text{eff}}] \tag{6}$$

where N_x, N_y, N_z are the demagnetization factors of the sample. These demagnetization factors depend on the geometry of the sample and affect the shape anisotropy. For a flat sample and in case of $B_0 \,||\, \hat{z}$ perpendicular to the plane of the sample (oop configuration), the in-plane factors are zero, $N_x = N_y = 0$, and the out-of-plane factor equals unity, $N_z = 1$. The Kittel equation for the out of plane geometry is given by:

$$\omega_0 = \gamma(B_0 - \mu_0 M_{\text{eff}}) \tag{7}$$

For the in-plane configuration, B_0 is parallel to the sample plane, and we receive $N_x = N_z = 0$ and $N_y = 1$ which results in:

$$\omega_0 = \gamma[B_0(B_0 + \mu_0 M_{\text{eff}})]^{\frac{1}{2}} \tag{8}$$

However, there might several resonances. Multiple spin wave modes are one explanation. The sample has a certain width d and the spin deflection has boundary conditions. Assuming that the spin excitation are pinned at the top- and bottom interfaces of the boundaries of the sample, the spins can only be excited in between. This is referred to as pinned boundary conditions. For the ferromagnetic resonance (FMR), all the spins precess in phase. The FMR (mode number n=0) is characterized by a single antinode as shown in Fig. 2.

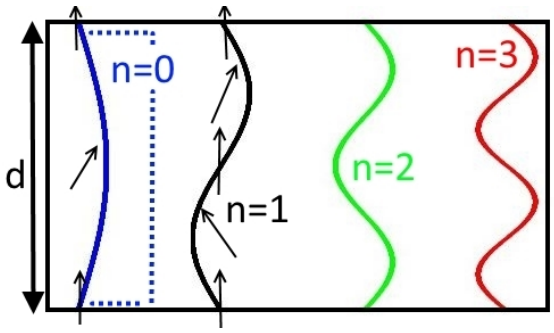

Figure 2: Schematic depiction of the first 3 sinusoidal PSSW modes and the FMR for pinned boundary conditions. The black box indicates the sample cross-section with a thickness d. For the first two modes, n=0 and n=1, the spin deflection is illustrated by the black arrows. Each line symbolizes the deflection of the spins, which is zero at the boundaries (pinned boundary conditions). Without these boundary conditions the deflection of the FMR (n=0) would be uniform, which is indicated by the dotted line.

Without pinning at the interfaces, the precession would be uniform throughout the sample thickness (dotted line), so that the FMR is also referred to as the uniform mode. Other

modes can also fulfill the pinned boundary conditions. The next possible mode (n=1) is characterized by antinodes at $\frac{d}{4}$ and $\frac{3}{4}d$ and nodes which are not only at the boundaries, but also in the middle of the sample. Figure 2 shows a depiction of the first three standing sinusoidal spin wave modes that can be obtained for pinned boundary conditions. These modes are referred to as "Perpendicular Standing Spin Waves" (PSSW) [6].
Microwave irradiation can not only excite the FMR but also the spin wave modes. For exchange spin waves and for a spin wave wave vector $k \ll \frac{2\pi}{a}$ with the lattice constant of the crystal a, the spin wave energy and thus frequency is approximated by

$$\hbar\omega = D_s k^2 \tag{9}$$

with the spin wave stiffness $D_s = (\frac{A}{M_s}) \cdot 2 \cdot g \cdot \mu_B$ and the exchange constant A. The wave vector is quantized over the film thickness d by $k = \frac{n\pi}{d}$ and n half-wavelength within the film. For the oop-configuration, the FMR resonance frequency $\omega_{\text{res, FMR, } k=0}$ is given by (7) and the spin wave resonance field is correspondingly given by

$$\omega_{res}(k) = \omega_{\text{res, FMR}} + \frac{D_s}{\hbar} \cdot k^2 \tag{10}$$

In Figure 3, we plot this simple parabolic spin wave dispersion for several values of the external field, which shifts the entire spin wave dispersion to higher frequencies. In case of PSSW, the actual dispersion relation is more complex since a group velocity $\frac{d\omega}{dk} = 0$ is required because of the thin film thickness.

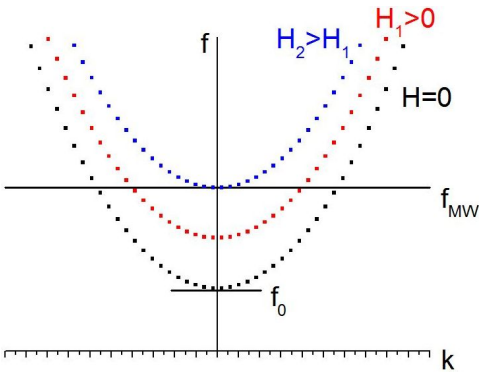

Figure 3: Quadratic spin wave dispersion for different strengths of the external magnetic field, which shifts the spin wave dispersion to higher frequencies. For a fixed microwave frequency (horizontal line), modes with $k > 0$ are excited at lower H_0 than the FMR (k=0).

The horizontal line in Fig. 3 indicates the measurement at a fixed microwave frequency. Assuming discrete $k = \frac{2\pi n}{d}$ with $n = 1, 2, 3...$ and a film thickness d, the PSSW modes will

be excited at successively lower values of the external magnetic field than the FMR. The quantitative difference between the resonance field of the FMR (n=0) and the resonance field of a PSSW with a mode number of n is given by the following formula [6]:

$$\mu_0 H_0^{\mathrm{res}}(n) - \mu_0 H_0^{\mathrm{res}}(n=0) = \Delta\mu_0 H_0^{\mathrm{res}}(n) = -D\frac{\pi^2}{d^2}n^2 \tag{11}$$

with the exchange stiffness D. For Yittrium Iron Garnet $D = 5.32 \cdot 10^{-7}$ T $\cdot$ m^2 [7] .

2.2 Measurement Setup

The excitation of magnetization dynamics using the broadband ferromagnetic resonance technique requires the placement of the sample in a static external magnetic field as well as an excitation by a microwave frequency magnetic field. A broadband detection of the FMR can be done with coplanar waveguides (CPW). To deliver the microwave magnetic field to the sample, either a microstrip or a coplanar waveguide is used. Figure 4 illustrates a coplanar waveguide (CPW).

The commercially available coplanar waveguides, used in this thesis, have been lithographically defined on a Rogers RO4003 printed circuit board with a thickness of $d = 0.25$ mm ($\epsilon_r = 3.55$, range from 8GHz-40GHz) [8]. The CPW structure on the top side of the substrate consists of a center conductor enclosed by ground planes to both sides. Compared to a coaxial cable the center conductor corresponds to the inner conductor and the ground planes correspond the the outer conductor. An alternating voltage V_1 with a microwave frequency f is applied to one end of the center conductor. On the other end the voltage V_2 is measured. According to Biot-Savart, the current through the center conductor leads to a magnetic field h. Since the center conductor is not circular but rectangular, the field lines are rather elliptical [9]. Based on the microwave field f, the magnetic field h oscillates.

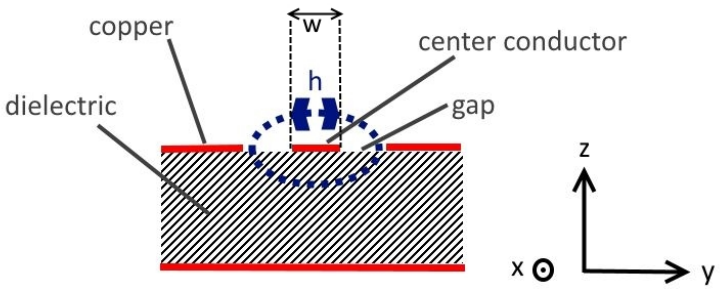

Figure 4: Schematic cut through a coplanar waveguide. A microwave current, flowing along x through the center conductor (with width w), generates a microwave frequency magnetic field h. Above the center conductor: $h \,||\, y$.

The sample on top of the CPW interacts with this field, which results in a varying transmission through the CPW, and thereby in a varying V_2. Characteristic dimensions of this CPW structure are the center conductor width w, the gap size, the thickness of the dielectric, the metalization thickness and the overall length [10].

The sample itself is positioned on the waveguide as shown in Fig. 5 and fixated with a glue, "Fixogum". The external static magnet field can either be orientated perpendicular to the sample plane (oop), or parallel to the sample plane (ip). In this thesis we will only use the out-of-plane configuration for the measurements. The strength of this static field is determined by a Hall-probe.

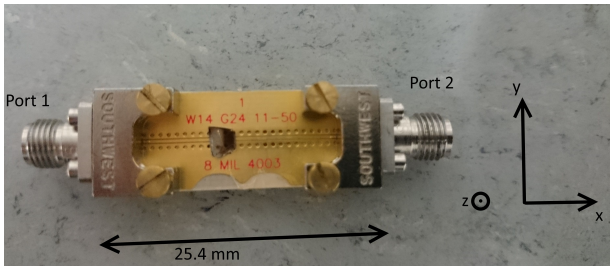

Figure 5: Measurement setup (top view), excluding the magnetic field. The sample is on the waveguide which can be connected to the vector network analyzer (or to the microwave source and the detector diode) by end-launchers. The static magnetic field is perpendicular to the photo plane for the oop configuration.

A vector network analyzer (VNA, Agilent Technologies, PNA-X, N5242A) or a microwave source (Agilent Technologies, E8257D) are used to apply a continuous wave electromagnetic signal to the CPW which generates the microwave driving field h. The frequency bandwidth of the setup is 10MHz $\leq f \leq$ 40GHz. Furthermore, the waveguide with the sample is positioned in a static and homogeneous magnetic field. Its maximal magnitude is $\mu_0 H_0 \approx 2$T. Figure 5 shows this setup, excluding the magnetic field. The static magnetic field would be aligned parallel to the z-axis for the oop-configuration and thus perpendicular to the photo plane. The waveguide is connected to the microwave source and the detector diode or the VNA via end-launchers and microwave cables.

A VNA is a standard tool to investigate high-frequency issues. It is used to apply a sinusoidal electromagnetic wave $V_1 \sin(\omega t)$ with amplitude V_1 to port 1 of the CPW and to measure the amplitude and the phase V_2 of the signal $V_2 \sin(\omega t)$ transmitted through port 2. The measured signal is then compared to the original output signal. The complex voltage ratio $\frac{V_2}{V_1} = S_{21}$ is returned by the VNA. So the VNA detects both, the amplitude difference and the phase difference. Therefore always both, the real and the imaginary part is shown. This setup is shown in Fig. 6. To suppress noise, the VNA is operated at small bandwidths ($<$ 10Hz).

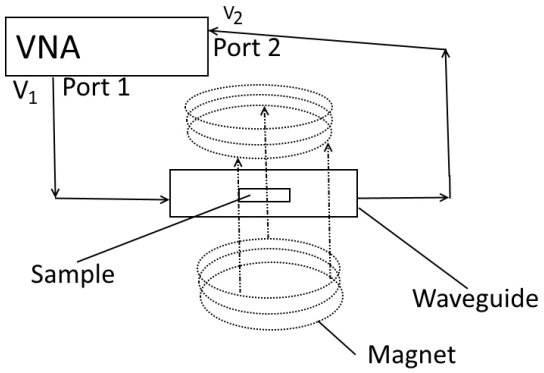

Figure 6: Measurement setup using a vector network analyzer (VNA). For drawing reasons the magnet field is in the plane of the sample, so the in-plane configuration is shown. The VNA compares the input sinusoidal electromagnetic wave V_1 with the measured signal V_2 and determines the complex voltage ratio $\frac{V_2}{V_1} = S_{21}$.

The VNA can alternatively also be used to measure the voltage reflected at port 1, which is referred to as an S_{11} measurement. The standard unit of the magnitude of $|S_{21}|$ is dB. It is converted by:

$$|S_{21}|\,[\mathrm{dB}] = 20 \cdot \log_{10}(|S_{21}|\,[1]) \tag{12}$$

Figure 7 shows a typical spectrum for this setup in which we plot S_{21} versus the static external field. It consists of the real and the imaginary parts. Each peak indicates a resonance. The real and the imaginary part show the same peaks.

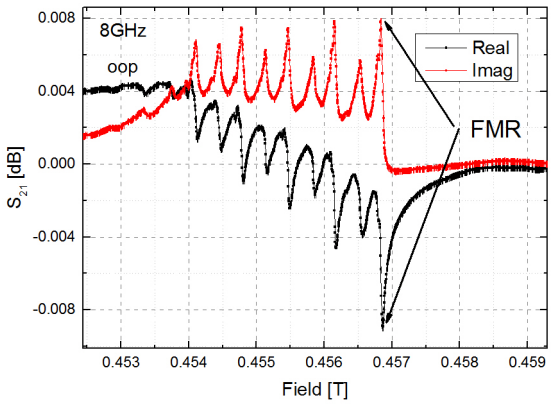

Figure 7: Typical spectrum for the VNA setup. It consists of the real and imaginary part of the transmission parameter S_{21}. Each peak indicates a resonance. Both curves show the same resonances. The FMR is the resonance with the highest magnetic field.

An alternative setup based on a lock-in amplifier and a microwave source is shown in Fig. 8. The microwave source is connected to port 1 and its output frequency is sinusoidally modulated with a modulation depth Δf_{mod} at a modulation frequency $f_{\mathrm{mod}} = 73\mathrm{kHz}$.

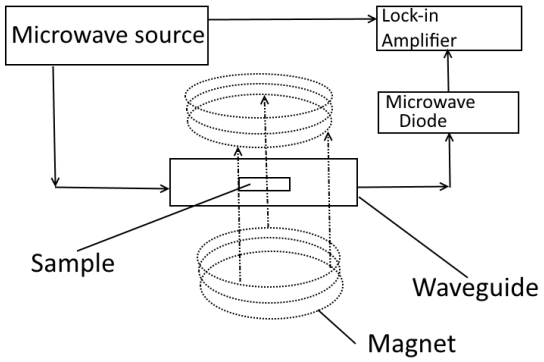

Figure 8: Measurement setup for the broadband FMR measurements, using a frequency modulated microwave source, a microwave diode and a lock-in amplifier. For drawing reasons the magnet field is in the plane of the sample, so the in-plane configuration is shown.

The output power P_{MW} can be varied in the range $-30\mathrm{dBm} \leq P_{\mathrm{MW}} \leq +30\mathrm{dBm}$. The transmitted signal at port 2 is rectified by a broadband microwave diode with a bandwidth of 40 GHz. The diode outputs a voltage $V_d \propto P_{\mathrm{MW}}$ in a first approximation. A lock-in amplifier multiplies the diode voltage with a reference signal at f_{mod} and integrates the result over a certain time. This results in a DC voltage. In this voltage the portion of signals which are not at the same frequency as the reference signal is close to zero. Thereby, only signals that are modulated at f_{mod} generate an output. For an input signal $V_D(s)$ the output signal is given by

$$V_{\mathrm{out}}(t) = \frac{1}{T}\int_{t-T}^{t} \sin(2\pi f_{\mathrm{mod}} \cdot s + \Delta\phi) V_{\mathrm{D}}(s)\,\mathrm{d}s \tag{13}$$

with the phase offset $\Delta\phi$ set to zero. Unlike the VNA setup, this setup is not phase-sensitive.

Figure 9 a) shows an illustration of a typical spectrum for this setup. This setup does not measure the transmission, but its derivation. Therefore, the resonance is indicated by the zero-crossing between to peaks.

In order to determine the resonance field, the microwave frequency is kept constant and the magnitude of the static external magnetic field is swept. The measured voltage is proportional to the derivative of the flux Φ in the sample, which is again proportional to the susceptibility [2]

$$V_{\mathrm{ind}} = -\frac{d\Phi}{dt} \propto m_y \propto \chi_{yy}(H_{\mathrm{eff}}, \alpha) h_y \tag{14}$$

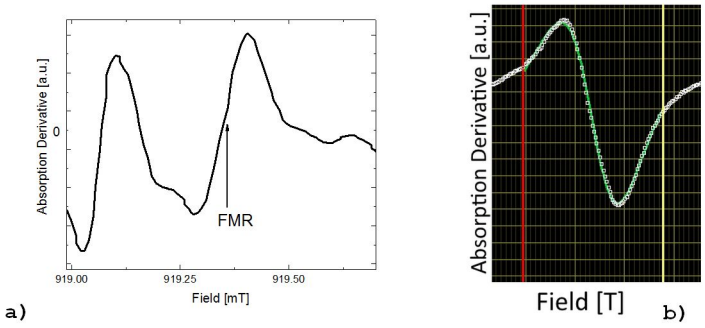

Figure 9: a) Typical spectrum for the lock-in amplifier setup. It measures the derivation of the transmission. Therefore, a resonance is indicated by the zero-crossing between two peaks (marked by the arrow). The FMR is the resonance with the highest magnetic field. b) A fit of the FMR using Eq. (18). The white points are measured, the green line is the fit. The yellow and red line indicate the fit area.

The susceptibility depends on the effective field H_{eff} and the damping parameter α. H_{eff}, in turn, depends on the effective magnetization M_{eff} and anisotropies. Following the Kittel equation (6), M_{eff} can be related to the resonance field H_{res}, whereas α is related to the Full Width Half Maximum (FWHM) ΔH of the resonance peak

$$V_{\text{ind}} \propto \chi_{yy}(H_{\text{res}}, \Delta H) \tag{15}$$

The lock-in amplifier derives the susceptibility over the magnetic field

$$V_{\text{LI}} \propto \frac{d\chi_{yy}(H_{\text{res}}, \Delta H)}{dH} = |\tilde{\chi}(H_{\text{res}}, \Delta H)| \tag{16}$$

To determine the resonance field and the FWHM of the resonance line, the resonance peaks are fitted with Levenberg-Marquardt optimization of

$$\text{VNA}: \; S_{21}(H_{\text{res}}) = \sum_j A_{(j)} e^{i\phi(j)} \chi_{yy}^{(j)}(H_{\text{res}}, \Delta H) + C_1 + C_2 H_{\text{res}} \tag{17}$$

$$\text{lock-in}: \; V_{\text{LI}}(H_{\text{res}}) = \sum_j A_{(j)} e^{i\phi(j)} \, |\tilde{\chi}(H_{\text{res}}, \Delta H)| + C_1 + C_2 H_{\text{res}} \tag{18}$$

with the parameters A and ϕ, and the values of interest ΔH and H_{res}. C_1 and C_2, the complex offset and slope, are included for technical reasons [2]. A fit for a lock-in detection measurement is shown in Fig. 9 b).

3 Analysis of Different Waveguides

3.1 Characterization

The waveguide is a central part of the measurement setup as it is used to provide the high-frequency electromagnetic field to the sample. It needs to exhibit low losses over the entire frequency range, also in the presence of a magnetic sample. In this chapter we analyze three different waveguides by a broadband transmission scan.

Three different waveguides are characterized and evaluated using the VNA measurement setup (Fig. 6): a thin coplanar waveguide (CPW), a wide one and a microstrip. Thin and wide, respectively, refer to the width w of the center conductor of the CPW. The thin and wide waveguides are CPW. These have an extended ground plane below the dielectric in addition to the ground planes on top of the dielectric, next to the signal line (see Fig. 4). Thus, the magnetic field component of the electromagnetic wave is in-plane and symmetric about the signal line. In contrary, the microstrip is missing the ground planes on top of the dielectric, so the magnetic field component of the electromagnetic wave is dominantly perpendicular to the plane. The dimensions of the investigated waveguides are given in Table 1.

	Thin CPW	**Wide CPW**	**Microstrip**
length	25.4 mm	25.4 mm	25.4 mm
width	12.7 mm	12.7 mm	12.7 mm
dielectric thickness	0.25 mm	0.25 mm	0.25 mm
metalization thickness	35 μm	35 μm	35 μm
center conductor width	340 μm	1.14 mm	1.14 mm
gap size	135 μm	480 μm	-

Table 1: Dimensions of the investigated waveguides. Note that only the center conductor width and the gap size are different. Since the microstrip has no ground planes beside the center conductor, no gap size is defined.

In order to minimize system errors, especially those of the cables, the setup has to be calibrated before the actual measurement. We use a Hewlett Packard Calibration Kit (85052C). Therefore, an open (creating an open circuit), a short (creating a short circuit) and a load of 50Ω are connected to the end of the cables, which the waveguide will be connected to (port 1). The S-parameters are measured for the whole frequency range up to 38.8GHz, which

is the maximum frequency of the used calibration kit. The same procedure is done with the second cable (port 2). Lastly, both cable ends are connected by a "unknown through", a connection whose parameters are not known. The same measurement is repeated. Then the VNA automatically calculates and applies the calibration. In order to utilize the exact calibration values for the specific frequencies, it is important to measure with the same frequency resolution as for the calibration.

Now the waveguides are connected to the cables. Again we measure the unknown through of the calibration for comparison. Thereby we can identify artifacts of the calibration, which are not caused by the waveguides, but are also seen in their spectra. The $|S_{21}|$ parameters measured for the three different waveguides are shown in Fig. 10. The applied power of the VNA is 0 dBm.

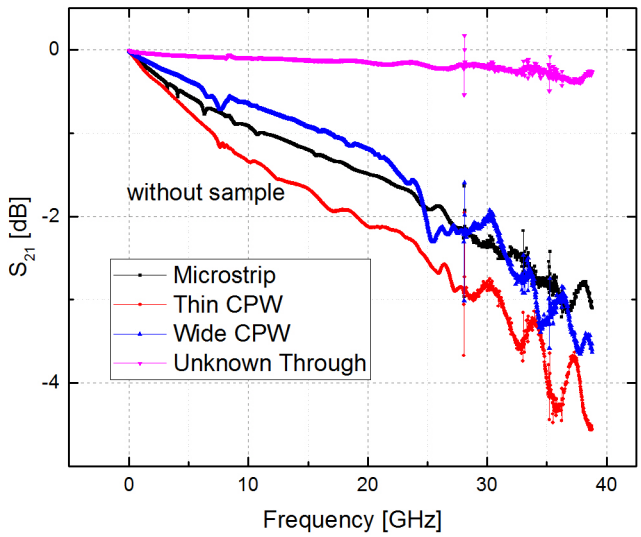

Figure 10: S_{21} versus frequency for the three different waveguides obtained by a calibrated VNA measurement. The VNA power is 0 dBm. To identify artifacts of the calibration, the transmission of the unknown through, with which the calibration was done, is shown as well. The resonance at about 27 GHz, which is visible for all waveguides, is such an artifact.

The sharp resonance at about 27 GHz is visible for all waveguides. It is an artifact of the calibration as it is also visible in the transmission measurement of the unknown through used for calibration. For frequencies below 22 GHz, the transmission is best with the wide CPW. Above this threshold, the microstrip shows a rather linear response while both CPW show large fluctuations. Below 8 GHz, the transmission through the microstrip shows three small resonances that are not present for the two CPW. However, both CPW show a resonance at

7.5 GHz. The resonance is very small for the thin CPW, whereas the wide CPW shows a large resonance. The area of the linear decrease of the transmission signal is largest for the thin CPW because it remains linearly up to 25 GHz.

For the broadband ferromagnetic resonance measurements, it is important to characterize the waveguide transmission also in the presence of a typical sample. The measurement of an Yttrium Iron Garnet (YIG) sample with a thickness of 2 μm, a width of 3.87 mm and a length of 3.29 mm and grown by liquid phase epitaxy (LPE) on gadolinium gallium garnet ($Gd_3Ga_5O_{12}$, GGG) substrate is evaluated and shown in Fig. 11. The measurement was done without the application of an external magnetic field. The transmission measurements in the presence of the sample reveal similar S_{21} versus frequency for all three waveguides.

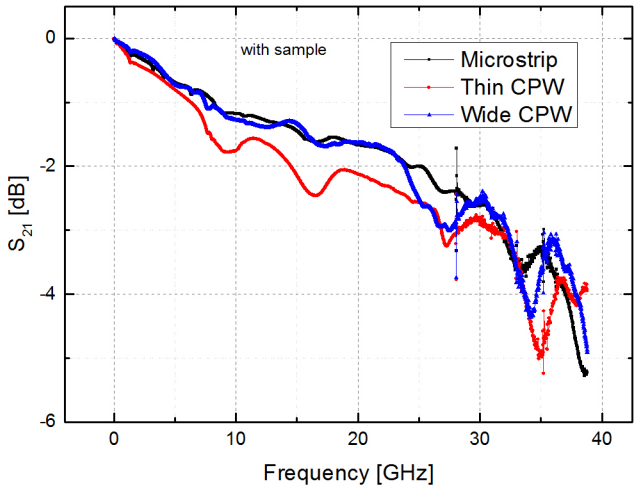

Figure 11: S_{21} versus frequency for the three investigated waveguides in the presence of a magnetic YIG sample. The measurement was done without the application of an external magnetic field. As in the figure without the sample (Fig. 10), we observe an artifact of the calibration at about 27 GHz.

To investigate the effect of the sample on the waveguide transmission completely, we calculate the losses caused by the sample with the following equation

$$\text{Signal loss} = S_{21,\ waveguide\ i}^{without\ sample} - S_{21,\ waveguide\ i}^{with\ sample} \tag{19}$$

Figure 12 illustrates this relations. Below 30 GHz, the additional losses caused by the sample are for all waveguides below 1 dB. Only at the highest frequencies, slightly larger losses in the microstrip become apparent.

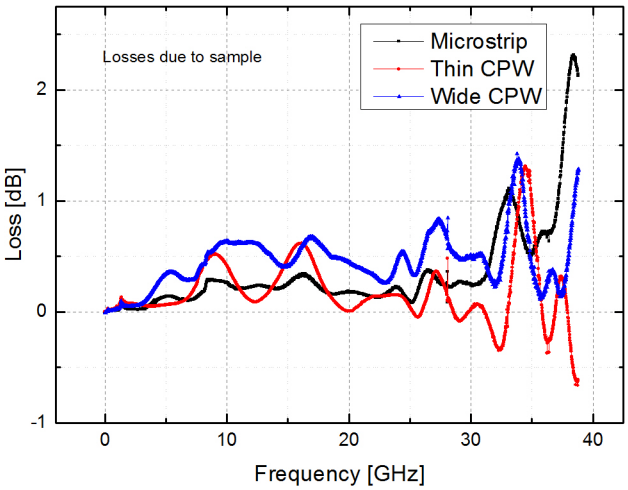

Figure 12: Losses caused by the sample. In order to investigate the impact of the sample, we subtract the transmission in presence of the YIG sample (Fig. 11) from the transmission of the single waveguides (Fig. 10) using Eq. (19). The sharp line at about 27 GHz is an artifact of the calibration.

3.2 Conclusion

Summing up, the transmission characteristics of all waveguides show low losses. Up to 38.8 GHz the losses remain lower than 5 dB. Up to about 30 GHz no significant resonances are observed. However, small resonances between 4 and 8 GHz have been recorded for the wide CPW and the microstrip. When measuring a sample, these resonances will also be seen and might distort the results. Loading the waveguides with a typical YIG sample, causes only modest additional losses. We chose the thin waveguide ($w = 340$ μm) for our measurements: It shows no noteworthy resonances below 25 GHz and its magnetic microwave component is mainly in plane.

4 Broadband Detection of Magnetization Dynamics

4.1 Broadband Determination of Magentic Resonance Fields and Line Widths

In this chapter we discuss a typical FMR spectra using a VNA measurement setup (Fig. 6) and the out-of-plane configuration.

While the microwave frequency is kept fix, we vary the static magnetic field, which is perpendicular to the sample plane (out-of-plane configuration). A typical FMR spectrum measured with a VNA, i.e. S_{21} as a function of the external magnetic field is shown in Fig. 13 a). The measured sample is a yittrium iron garnet (YIG) sample with a thickness of 2 μm, a width of 3.87 mm and a length of 3.29 mm. The microwave frequency is 8 GHz and the applied power 0 dBm. We do not only observe one resonance (peak) but several. The FMR is the one with the highest static field as shown in Chapt. 2.1 on page 2.

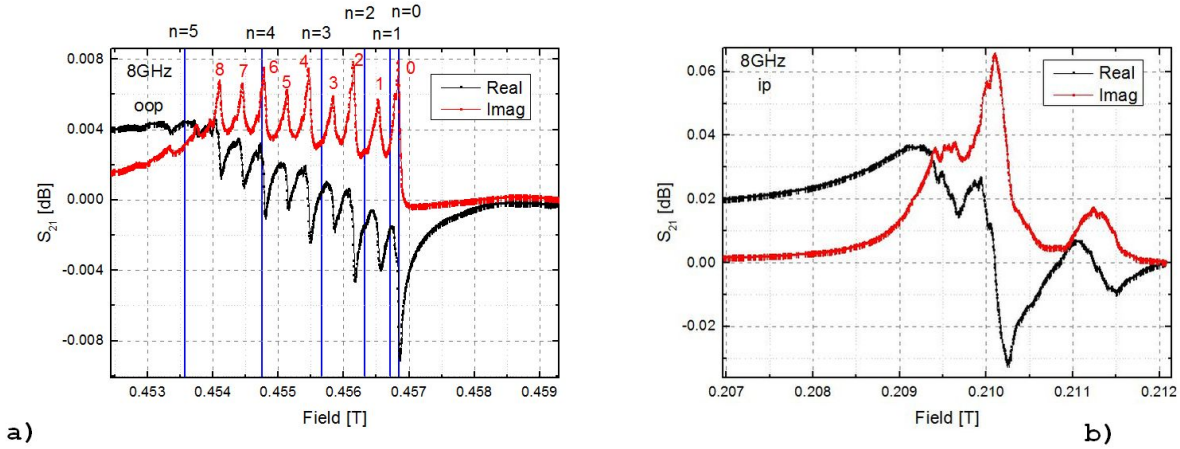

Figure 13: a) A typical "out-of-plane" FMR spectrum for a 2 μm thick YIG sample measured with a VNA, a microwave frequency of 8 GHz and a microwave power of 0 dBm. Each peak indicates a resonance. The blue lines indicate the PSSW modes. The FMR is the mode for n=0. The strong resonances are enumerated in red. b) A typical "in-plane" spectrum for a 2 μm thick YIG measured with a VNA, a microwave frequency of 8 GHz and a microwave power of 0 dBm.

Assuming, the other resonances might be Perpendicular Standing Spin Waves (PSSW), we calculate the field offset between putative PSSW and the FMR at a specific frequency following Eq. (11). These field values are indicated by the blue lines. At these particular

field values, some very tiny peaks are present. However, the strong resonances can not be explained with PSSW. These are probably caused by inhomogeneities within the sample.

The additional resonance modes are enumerated in red. Their field offset to the FMR is evaluated ($B_{res}(n)$-$B_{res}(0)$) based on the experimental data for a microwave frequency of 8 GHz and 21 GHz and plotted in Fig. 14. The calculated offsets of the PSSW are also shown. The offset of the strong resonance modes has a linear decrease in the resonances fields versus the mode numbers, in contrary to the quadratic decrease of the PSSW.

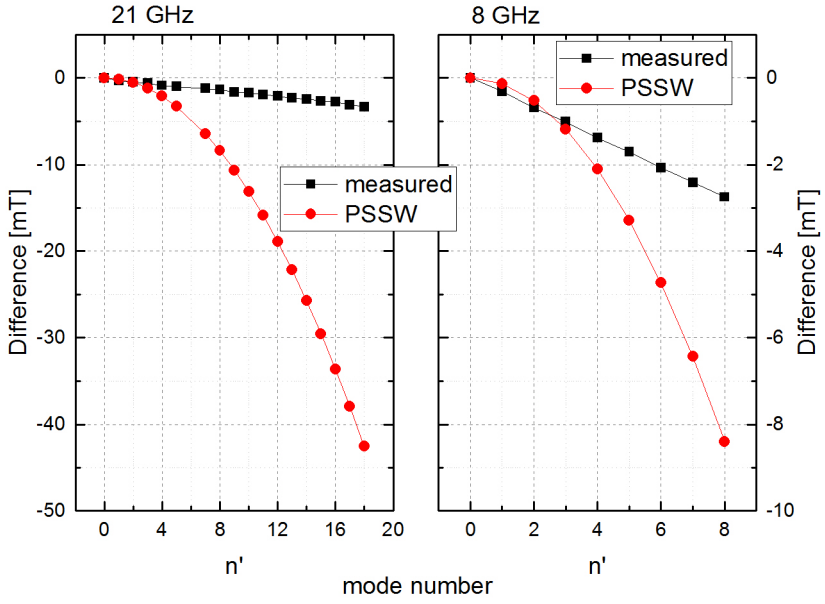

Figure 14: Higher order mode offset. The field difference between the observed higher order resonances and the FMR is calculated: $B_{res}(n)$-$B_{res}(0)$ and plotted (black) for a microwave frequency of 8 GHz and 21 GHz. Furthermore, the calculated offsets of the PSSW (Eq. (11)) are shown (red). So, the strong resonance modes seen in Fig. 13 are no PSSW.

Our previous discussion were referred to magnetic resonance spectra recorded with the magnetic field in out-of-plane direction. But changes in the setup enable the static field to be in the same plane as the sample (in-plane configuration). The results for 8 GHz are shown in Fig. 13 b). We observe less resonances. The resonances caused by the inhomogeneity of the film are closer together in this geometry. They can not be separated anymore and a wide resonance peak becomes visible.

4.2 Evaluation of Measurement Results

4.2.1 Resonance Field

Based on the measured out-of-plane spectra for several microwave frequencies (broadband FMR), we can determine the effective magnetization $M_{\text{eff}} = M_{\text{s}} - H_{\text{k}}$[1], the gyromagnetic ratio γ and the Lande g-factor g as well as the damping parameter α and the "inhomogenous broadening" ΔH_0.

Based on the Landau-Lifshitz-Gilbert equation (3) and the Kittel equation (6), we start with the out-of-plane relation between the microwave frequency and the static magnetic resonance field (Eq. (7))

$$\frac{\omega}{|\gamma|} = \mu_0(H_{\text{res, 0}} - M_{\text{eff}}) \tag{7}$$

in which ω is the angular frequency, γ is the gyromagnetic ratio and $H_{\text{res, 0}}$ is the FMR resonance field [11]. On the other hand, the gyromagnetic ratio is related to the Lande g-factor g. According to Eq. (7), a linear dependency between the microwave frequency and the static magnetic resonance field is given. If we plot $B_{\text{res, 0}}$ versus the applied microwave frequency f for every single measurement (Fig. 15), we can extract the magnetic parameters of the sample.

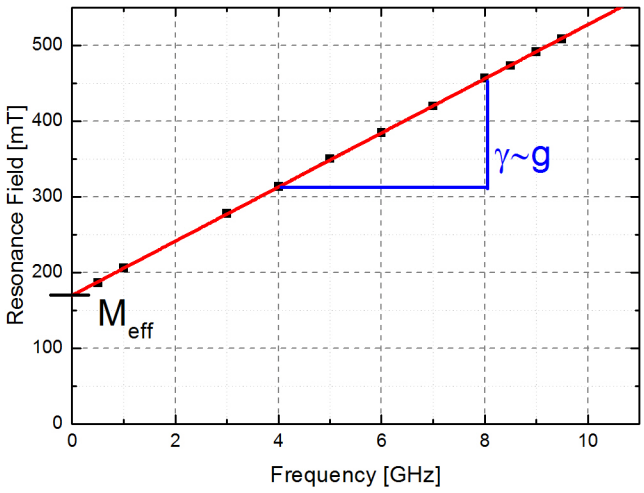

Figure 15: Resonance field versus frequency. The resonce field is plotted versus the frequency and a linear fit is performed. Thereby M_{eff} (offset), and g (slope) can be calculated. The applied VNA power is 0 dBm.

[1] M_{s} is the saturation magnetization and H_{k} is the out of plane anisotropy field.

In order to apply Eq. (7) on Fig. 15, we solve the equation for the resonance magnetic flux density $B_{\text{res, 0}}$ and get the following relation

$$B_{\text{res, 0}} = \mu_0 \cdot H_{\text{res, 0}} = \frac{\omega}{|\gamma|} + \mu_0 M_{\text{eff}} = \frac{2\pi}{|\gamma|} f + \mu_0 M_{\text{eff}} \tag{20}$$

Thus, the slope of a linear fit $B_{\text{res, 0}} = a + b \cdot f$ is given by

$$b = \frac{2\pi}{|\gamma|} = \frac{2\pi\hbar}{\mu_B} \cdot \frac{1}{g} \tag{21}$$

The effective magnetization can be calculated from the intersect

$$a = \mu_0 M_{\text{eff}} \tag{22}$$

For this measurement, a magnet with wide pole shoes and a small gap (gap/diameter $\approx$ 1/5) is used in order to generate a homogeneous field. However, its maximum field is limited to about 0.5 T. For YIG, this enables FMR measurements at microwave frequencies up to 9.5 GHz. Eleven transmission spectra for frequencies between 0.5 Ghz and 9.5 GHz are taken and the corresponding FMR field and the Full Width Half Maximum (FWHM) of the resonance peak are determined using the fit of Eq. (17). The VNA power is set to 0 dBm.

We apply a linear fit on Fig. 15 and use Eq. (21) and (22). The measured effective magnetization of $M_{\text{eff}} = (135.111 \pm 0.475)\frac{\text{kA}}{\text{m}}$ is close to the expected saturation magnetization $M_{\text{s}} = 140\text{kA/m}$ [12]. This means there are only small perpendicular magnetic anisotropies. The gyromagnetic ratio is the ratio between the angular momentum and the magnetic moment. From the fit, we obtain $\gamma = (1.757 \pm 0.005) \cdot 10^{11}\ \text{s}^{-1}\ \text{T}^{-1}$.
From the gyromagnetic ratio we can derive the Lande g-factor and get $g = 1.999 \pm 0.005$. These values are in good agreement with the values evaluated for other YIG samples [12], [13].

4.2.2 Full Width Half Maximum of the Resonance Peak

To determine the Gilbert damping parameter α and the inhomogeneous broadening ΔH_0, we plot the resonance line width versus the applied frequency. The magnetic susceptibility in Eq. (4) contains the resonance line width ΔH. From the LLG (Eq. (3)), ΔH is related to the damping α by [5]

$$\Delta H = \frac{4\pi\alpha}{|\gamma|\,\mu_0} \cdot f \tag{23}$$

However, the LLG does not include non-Gilbert contributions to the line width. Following common practice, we phenomenologically include the so-called "inhomogenous broadening" by

$$\Delta H = \frac{4\pi\alpha}{|\gamma|\,\mu_0} \cdot f + \Delta H_0 \tag{24}$$

The damping α is deduced from the slope of ΔH versus f and the inhomogenous broadening ΔH is the intersect. The Full Width Half Maximum of the FMR peaks is plotted over the applied microwave frequency in Fig. 16.

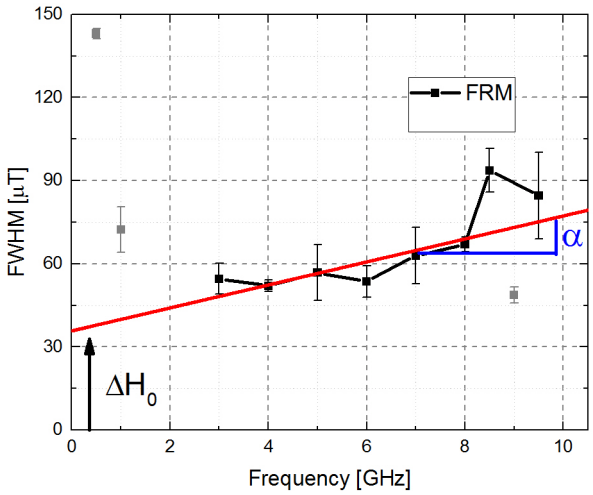

Figure 16: Damping. The Full Width Half Maximum (FWHM) of the FMR peaks are plotted versus the microwave frequency. The damping parameter α is calculated based on the slope of a linear fit (red line) and the inhomogeneous broadening ΔH_0 is its offset. The grey values have not been considerd for the fit since they show big discrepancies.

However, it is very difficult to determine the actual FWHM of the FMR peak. Dependent on the choice of the fit area, the calculated FWHM are different. It is not clear which fit area is best and which measured points do not belong to the FMR anymore. Therefore, the two most extreme widths are determined and their average is plotted. Thus, the measuring points are effected by substantial errors and not all points meet the linear expectation. Especially, the points below 2 GHz and at 9 GHz show big discrepancies. Therefore, these points are not considered in the fit. The measuring points show a vague linear increase versus the microwave frequency. We receive $\alpha = (5.8 \pm 1.5) \times 10^{-5}$, which is rather small compared to the expected dimension of $\alpha \approx 10^{-4}$ [13]. However, this dimension has also been evaluated for some other YIG samples [14], and $\Delta H_0 = (35.8 \pm 6.2)\ \mu$T.

5 Determination of Adequate Microwave Source Parameters

5.1 Microwave Modulation Depth

In addition to the previously used measurement setup based on a VNA, we investigate another measurement setup based on the lockin-detection (Fig. 8). The accuracy of the measurement result is influenced by several measurement parameters. Here we investigate the influence of the applied microwave power and frequency modulation depth on the FMR spectra obtained using a 2 μm thick, a 3.87 mm broad and a 3.29 mm long YIG film which is grown on gadolinium gallium garnet substrate by liquid phase epitaxy.

For this measurement, a magnet with small pole shoes is used to reach high magnetic fields. The gap width is of the same dimension as the pole shoe diameter (gap/diameter $\approx$ 1). Therefore, the sample has to be positioned in the very middle of the room between the pole shoes in order to have a homogeneous field.

The frequency of the microwave driving field is modulated. This modulation is equivalent to a corresponding modulation of the external static magnetic field ΔH_{mod} and is given for a frequency modulation Δf_{mod} by (cf. Eq. (7))

$$\mu_0 \cdot \Delta H_{\mathrm{mod}} = \frac{2\pi \cdot \Delta f_{\mathrm{mod}}}{\gamma} \tag{25}$$

For ΔH_{mod} similar or larger than ΔH, the resonance line shape is distorted. On the other hand, the signal amplitude increases with increasing modulation depth. Hence, there is an optimal modulation depth. To determine this, we record FMR spectra at various modulation depths ranging from $\Delta f_{\mathrm{mod}} = 10$kHz to $\Delta f_{\mathrm{mod}} = 50$MHz and plot the measured signal curves in one diagram. In Fig. 17 we show normalized[2] FMR spectra, which are offset on the y-axis, for a microwave power of -20 dBm. The larger the modulation depth, the larger the offset. The spectra remain very similar for $\Delta f_{\mathrm{mod}} \leq 800$kHz. But the line broadens for larger modulation dephts.

We extract the line width from the measured spectra as shown in Fig. 18. The two peaks next to the resonance field are determined and their field difference is calculated.

[2]The spectra are normalized in order to eliminate impacts of the signal amplitude on the lineshape.

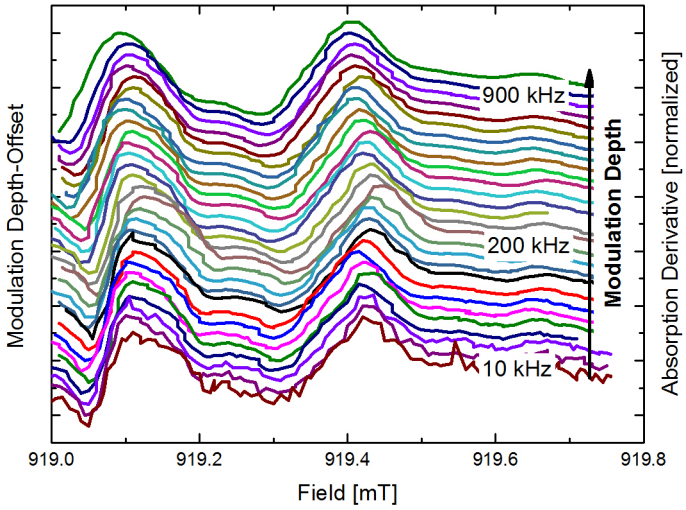

Figure 17: FMR spectra for the 2 μm thick LPE YIG film, recorded in the oop configuration at 21 GHz. The applied microwave power is -20 dBm. The FMR is the resonance at 919.4 mT. For lower fields, a further resonance is shown. The spectra were recorded at different frequency modulation depths. All spectra are offset on the y-axis with increasing positive offsets for larger modulation depths. The FMR line is distorted for modulation depths larger than about 800kHz.

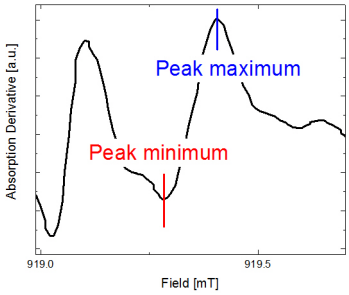

Figure 18: Schematic depiction of the peak-peak method. The width is determinated by the distance between the peak maximum and the peak minimum. This method is used to show how the line shape is influenced by the microwave modulation depth and the microwave power of the microwave source. We use this method, since the actual FWHM cannot be determined properly.

Note that the extraction of the line width from the peak-peak method is not equivalent to a determination of the true FWHM. We do not fit the resonance but only take in account the extremal points. Due to the presence of several resonances close to each other, fitting of the FMR line is not reliably possible. It is questionable which fit area is best and which measured points do not belong to the FMR anymore. Hence, a fit results in large uncertainties. Whereas the absolute values for the line widths are thus different from the true FWHM,

the approach is sufficient to determine the maximum reasonable modulation depth. In this chapter we will use the terms "(line) width" and "distance calculated by the peak-peak method" synonymously.

The line widths are plotted as a function of the modulation depth in Fig. 19 a). The top axis shows the equivalent magnetic field modulation using Eq. (25). The modulation frequency that is equivalent to the width of the resonance (0.12 mT) is illustrated by the blue line. Modulation depths greater than this line distort the lineshape as mentioned above.

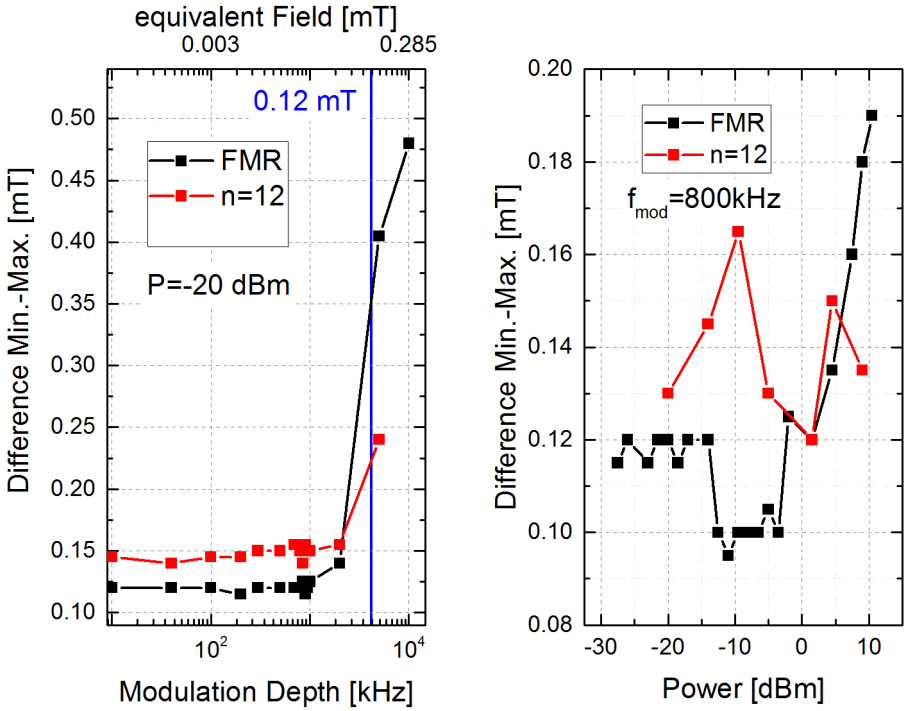

Figure 19: Width of the FMR and of n=12 for different modulation depths (a) and different powers (b). The equivalent power for the modulation depth is calculated according to Eq. (25). The modulation depth corresponding to the width of the resonance is marked by the blue line. Above the optimal modulation depth and power, respectively, the line width increases.

As expected, the width increases when the modulation depth is similar to the line width of the resonance (either in field or frequency). Beside the FMR, another mode (n=12) is evaluated to compare the results. For this higher mode and a modulation depths of 10 MHz there is no resonance visible anymore, so that a line width can not be determined.

Final measurements and the power evaluation in the following chapter base on the found optimum of $\Delta f_{\mathrm{mod}} = 800$ kHz.

5.2 Microwave Power

The applied power determines the strength of the microwave frequency driving field that again excites the magnetization dynamics (LLG (3)). At a large power and driving field, non-linear effects can distort the line shape. A low power may produce too little signal for detection and no sufficient signal to noise ratio. For an increasing microwave power, we expect a constant line width until a threshold. For a higher power, the driving field generates non-linear effects and the width increases.

We vary the microwave power from -30 dBm to +20 dBm for a fixed modulation depth of 800 kHz and a microwave frequency of 21 GHz. The measured spectra are normalized and plotted in Fig. 20.

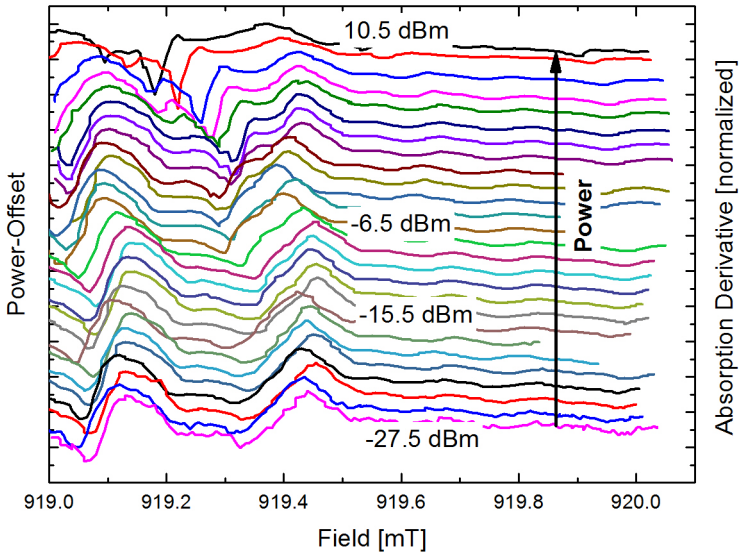

Figure 20: FMR spectra recorded for various microwave powers at $f = 21$ GHz and a modulation depth of $\Delta f_{\mathrm{mod}} = 800$ kHz. The FMR is the resonance at about 919.4 mT. The spectra are normalized and offset. The higher the power, the larger the positive y-offset. A power above around -6 dBm causes non-linear effects and the line width increases.

The spectra are very similar for $P_{\mathrm{MW}} \leq -6$ dBm. Then the peak width increases, which we relate to nonlinear effects. We extract the line width from all these curves as described above and plot them versus the microwave power P_{MW}. Figure 19 b) illustrates the width of the FMR (n=0) and of a higher mode (n=12), as done for the variation of the modulation depth. Up to about -5 dBm the line width fluctuates around 0.1 mT, however above -5 dBm it increases. In order to be close to the possible maximum power and to have some buffer left, the measurements are done with -7 dBm.

To discuss the power-dependence in a simple macro-spin model, we look upon the deflection angle θ (Eq. (5)). The linearized LLG (3) delivers

$$m_y = \overleftrightarrow{\chi} \cdot h_y \tag{26}$$

in which $\overleftrightarrow{\chi}$ is the complex susceptibility tensor and h is the high-frequency field which depends on the applied microwave power and drives the magnetization dynamics. In our experimental out-of-plane configuration, the m-precession is circular with $m_x = m_y = \chi_{yy} h_y$ and $h_x = h_z = 0$. With the susceptibility defined in Eq. (4) and the Kittel equation (6) we find $\chi_{yy} = \frac{M_s}{-i\Delta H}$ [5] in which M_s is the saturation magnetization and ΔH is the FWHM of the resonance line. We approximate h_y above the center conductor by $h_y = \frac{I}{2w}$, in which I is the current and $w = 340$ μm is the width of the center conductor. The microwave current I is related to the microwave power by $P_{\mathrm{MW}} = Z_0 \cdot I^2$ and the impedance $Z_0 = 50\ \Omega$. However, the power driving the magnetization dynamics is not the power P_{MW} of the microwave source, but the power P_0 reaching the sample on the CPW. Therefore, the applied power has to be corrected by the losses in the cable and in the waveguide. The former are specified in the given datasheet of the producer to be -2.6 dB at 21 GHz [15]. The latter has been measured in the Chapt. 3 [3] and is -0.65 dB. Therefore the finally applied power is: $P_0 = P_{\mathrm{MW}} - 2.6\ \mathrm{dB} - 0.65\ \mathrm{dB}$. Then the precession cone angle θ (cf. Fig. 1 and Eq. (5)) is given by the following formula

$$\frac{m_y}{M_\mathrm{s}} = |sin(\theta)| = \frac{1}{2 \cdot w} \cdot \frac{1}{\Delta H} \cdot \sqrt{\frac{10^{P_0}}{50\Omega}} \tag{27}$$

The conversion of P(dBm) to P(W) is given by $P(\mathrm{W}) = \frac{10^{\frac{P(\mathrm{dBm})}{10}}}{1000}$. In Fig. 21 we plot $(\sin\theta)^2$ as a function of P on a double logarithmic scale. The line is a fit to data for $P \leq 2 \cdot 10^{-4}$ W with a fixed slope of 1.

Hence, the line represents the linear dependency, where $(\sin\theta)^2 \propto P$. The maximum precession cone angle θ_{max} is the point with the highest power being still on the linear line. Our measurement yields $\theta_{\mathrm{max}} = 0.04°$.

[3] We take only half of the measured loss, since the sample is located in the middle of the waveguide

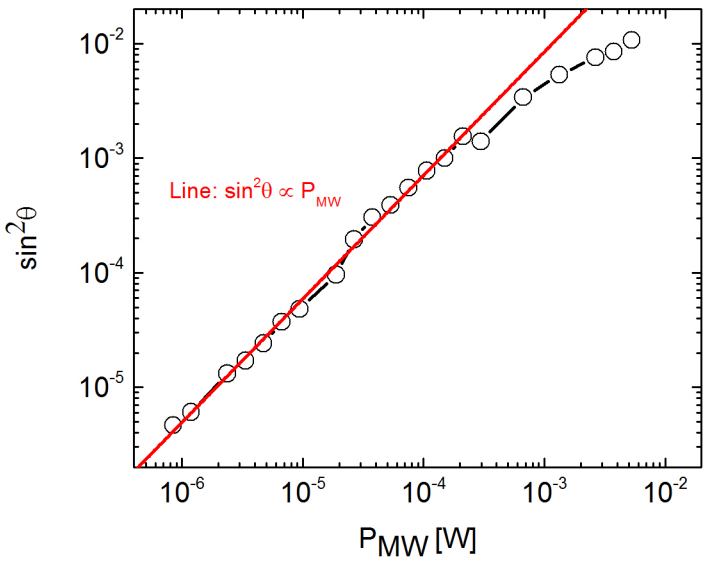

Figure 21: Magnetization precession cone angle as a function of microwave power recorded at f=21 GHz with a frequency modulation depth of $\Delta f_{\mathrm{mod}} = 800$ kHz. The straight line represents the linear dependency. For points not on this line anymore, non-linear effects become visible. The maximum precession cone angle, for which we are still in the linear regime, is $\theta_{\mathrm{max}} = 0.04°$.

6 Distance Dependent Measurements

6.1 Setup

In all previous investigations, the sample has always been positioned directly on the waveguide. Subsequently, we analyze the impact of different distances between waveguide and sample, using the lock-in amplifier setup (Fig. 8) and the oop configuration. Therefore, the position of the waveguide is fixed and the sample is positioned on the bottom of a brass holder whose distance to the waveguide can be varied by screws. This setup can be seen in Fig. 22. The distance is measured by a vernier caliper. Since the effective magnetization and the Lande g- factor are supposed to remain constant, we investigate the line width by the same method as in chapter Chapt. 5.

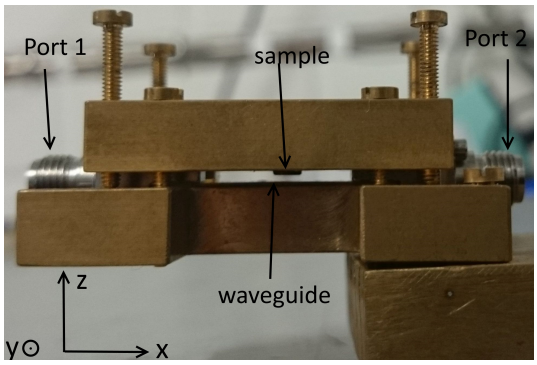

Figure 22: Measurement setup (side view) for variation of the sample distance. The sample can be seen directly below the holder, the waveguide is upon the lower metal. The screws vary the distance of the sample holder while the waveguide is fixed. The ports are connected to the microwave source and the diode. The magnetic field is aligned parallel to the z-axis.

6.2 Bulk YIG

We measure a Yttrium Iron Garnet (YIG) sample with a thickness of 2 μm, a width of 3.87 mm and a length of 3.29 mm, which is grown on gadolinium gallium garnet substrate by liquid phase epitaxy. We use the previously determined microwave modulation depth of 800 kHz and a microwave power of -7 dBm. Eight distances between 0 mm and 0.32 mm have been investigated. Figure 23 depicts the spectra for three different distances. The resonances

have slightly different shape, however, the general shape remains similar. Since the samples have different distances, the magnitudes of the microwave field is different for each of them. To avoid these influences, the spectra are normalized.

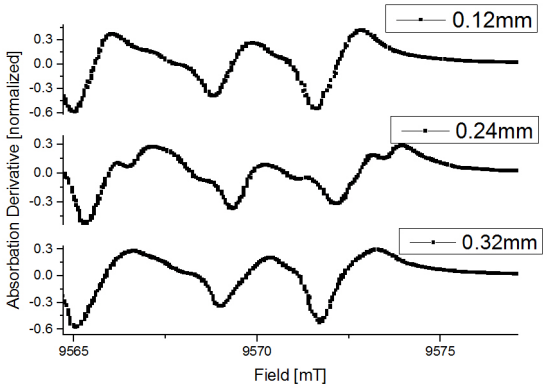

Figure 23: Distance dependence of the FMR line width for a microwave frequency of 21 GHz. Spectra for three different distances between the sample and the waveguide are shown. The modulation depth is 800 kHz and the power is -7 dBm. The spectra are normalized to avoid impacts of the signal magnitude. The resonances show slightly different line shapes, however, the general shape remains similar.

Again we observe several resonances close to each other, directly linked with problems concerning an appropriate fit of a resonance. The resonance area and the fit area can not be determined properly and lead to a big uncertainty in the fit. Nevertheless, it is possible to indicate whether and how the line width varies. Therefore, we consider the distance between the peak maximum and its minimum (see Fig. 18). A clear tendency in the distance development between the maximum and the minimum and consequently the damping can not be derived in our measurement, shown in Fig. 24.

Especially, the width at the distance of 0.24 mm is very difficult to determine since there are two tiny peaks close to each other and it is not possible to find out whether they are one big peak or only one of them is the FMR. Therefore, two points are shown, concerning this distance.

The problem might be found in the setup. Perhaps the distance between the metal of the sample holder and the waveguide has been to small. As the grounded waveguide has a metal layer below the dielectric, the brass might create "a second ground plane" and influence the signal.

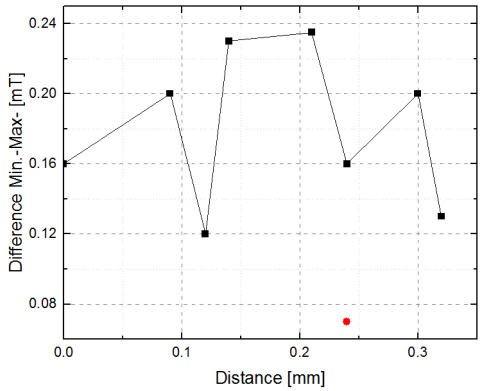

Figure 24: Distance dependence of the FMR line width. The distance between the sample and the waveguide is varied and the FMR line width is determined for a microwave frequency of 21 GHz. The modulation depth is 800 kHz and the power is -7 dBm. No clear tendency in the distance development can be derived. For a distance of 0.24 mm two points are shown because of two tiny peaks extremely close to each other. The distance is evaluated by the peak-peak method.

7 Summary and Outlook

In this thesis we considered two setups: one using a VNA and one using a lock-in amplifier. Relating to the three investigated waveguides, we found out that there are no big differences between their broadband transmission spectra. However, the thin CPW has little advantages and so we selected this one for our measurements. Important parameters for ferromagnets, such as the effective magnetization, the Lande g-factor and the damping parameter, have been evaluated with the VNA setup and are in good agreement with the expected values based on literature. For the setup using lock-in detection, we showed that the microwave frequency modulation depth and the microwave power of the microwave source have to be optimized before the final measurements can take place. Finally, the setup has been modified to vary the distance between the sample and the waveguide. We used the lock-in amplifier and the previously evaluated measurement parameters to determine the line width of a YIG sample. However, the result was not explicit enough to derive a clear tendency.

Future approaches to optimize the setup might be a computational simulation to vary the sizes of the waveguide. Since the waveguides can also be produced at WMI or TUM, its sizes can be individually optimized for the experiment. A COMSOL simulation has already been done during this study, however, the result was not satisfying since the computed values did not agree with the measured ones. In order to evaluate the above mentioned parameters in relation to the distance between the sample and the waveguide, a non-metallic sample holder could be used in order to prevent the existence of a second "ground plane". Furthermore, a extremely thin sample could be measured. For this sample no inhomogeneities are expected so that the FMR is very clear and can be fitted in a reliable way.

Bibliography

[1] O. Yalcin, *Ferromagnetic Resonance*, http://cdn.intechopen.com/pdfs-wm/45527.pdf (2013)

[2] L. Dreher, *Spin Mechanics in Paramagnetic and Ferromagnetic Materials*, Ph.D. thesis, Technische Universität München, 2013

[3] R. Gross, A. Marx, *Festkörperphysik*, 2. Auflage, De Gruyter, Berlin/ Bosten 2014

[4] T. Gilbert, *A phenomenlogoical theory of damping in ferromagnetic materials*, IEEE Trans. Mag. **40**, (2004)

[5] H.T. Nembach, T. J. Silva, J. M. Shaw, M. L. Schneider, M. J. Carey, S. Maat, and J. R. Childress, *Perpendicular ferromagnetic resonance measurements of damping and Lande g factor in sputtered* $(Co_2Mn)_{1-x}Ge_x$ *thin films*, Physical Review B **84**, 054424 (2011)

[6] C. Kittel, *Introduction to Solid State Physics*, 8. Edition, John Willey & Sons, Inc., 2005

[7] S. Klingler, A. V. Chumak, T. Mewes, B. Khodadadi, C. Mewes, C. Dubs, O. Surzhenko, B. Hillebrands, A. Conca, *Measurements of the exchange stiffness of YIG films by microwave resonance techniques*, J. Phys. D: Appl. Phys. 48 (2015)

[8] Rogers Corporation, *RO4000© series*, https://www.rogerscorp.com/documents/726/acm/RO4000-Laminates—Data-sheet.pdf

[9] Y. Ding, T. J. Klemmer and T. M. Crawford, *A coplanar waveguide permeameter for studying high-frequency properties of soft magnetic materials*, J. Appl. Phys. 96(5) (2004)

[10] Southwest Microwave, *Optimizing Test Boards for 50 GHz End Launch Connectors*, http://mpd.southwestmicrowave.com/showImage.php?image=439&name=Optimizing%20Test%20Boards%20for%2050%20GHz%20End%20Launch%20Connectors

[11] S. V. Vonsovskii, *Ferromagentic Resonance*, S. Monson Binding, Jerusalem 1964

[12] Deltronic Crystals Industries Inc., *Yttrium Iron Garnet*, http://deltroniccrystal industries.com/deltronic_crystal_products/yttrium_iron_garnet

[13] M. B. Jungfleisch, W. Zhang, W. Jiang, H. Chang, J. Sklenar, S. M. Wu, J. E. Pearson, A. Bhattachary, J. B. Ketterson, M. Wu, A. Hoffmann, *Spin waves in micro-structured yttrium iron garnet nanometer-thick films*, J. Appl. Phys. 117, 17D128 (2015)

[14] C. Hauser, T. Richter, N. Homonnay, C. Eisenschmidt, H. Deniz, D. Hesse, S. Ebbinghaus, G. Schmidt, *Yttrium Iron Garnet Thin Films with Very Low Damping Obtained by Recrystallization of Amorphous Material*, arXiv:1502.06724 (2015)

[15] True Blue©, *Low Loss Cable Assemblies* https://www.teledynestorm.com/pdf/True_Blue.pdf

Acknowledgement

I would like to express my gratitude to all people at Walther-Meißner-Institut who supported me during this thesis. I want to thank in particular:
PD Dr. Sebastian Gönnenwein for giving me the opportunity to work at WMI and on this very interesting topic.
Dr. Mathias Weiler for his great support, his supervision of this thesis and for all the ideas and explanations.
Stefan Klingler for his inexhaustible support during the measurements.
The **technical staff** of WMI, who were always very responsive and constructed all the required things in a short time.